

# Evaluation of a Compact Broadband Differential Absorption Lidar for Routine Water Vapor Profiling in the Atmospheric Boundary Layer

R. K. NEWSOM

*Pacific Northwest National Laboratory, Richland, Washington*

D. D. TURNER

*NOAA/Earth System Research Laboratory/Global Systems Division, Boulder, Colorado*

R. LEHTINEN

*Vaisala Oyj, Vantaa, Finland*

C. MÜNDEL

*Vaisala GmbH, Hamburg, Germany*

J. KALLIO AND R. ROININEN

*Vaisala Oyj, Vantaa, Finland*

(Manuscript received 15 June 2018, in final form 27 September 2019)

## ABSTRACT

The performance of a novel water vapor broadband differential absorption lidar (BB-DIAL) is evaluated. This compact, eye-safe, diode-laser-based prototype was developed by Vaisala. It was designed to operate unattended in all weather conditions and to provide height-resolved measurements of water vapor mixing ratio in the lower troposphere. Evaluation of the Vaisala prototype was carried out at the U.S. Department of Energy's Atmospheric Radiation Measurement site in north-central Oklahoma (i.e., the Southern Great Plains site) from 15 May to 12 June 2017. BB-DIAL measurements were compared with observations from radiosondes that were launched within 200 m of the BB-DIAL's location. Radiosonde measurements are also compared with observations from a collocated Raman lidar and an Atmospheric Emitted Radiance Interferometer. During the evaluation period, the BB-DIAL operated continuously and did not experience any failures or malfunctions. The data availability was greater than 90% below 900 m but then decreased rapidly with height above this level to less than 10% above 1500 m AGL. From 106 radiosonde profiles, the overall mean difference (averaged temporally and vertically up to 1500 m) between the BB-DIAL and the radiosonde was  $-0.01 \text{ g kg}^{-1}$ , with a standard deviation of  $0.65 \text{ g kg}^{-1}$ , and a linear correlation coefficient of 0.98. For comparison, the overall mean difference between the Raman lidar and the radiosonde was  $0.07 \text{ g kg}^{-1}$ , with a standard deviation of  $0.74 \text{ g kg}^{-1}$ , and a linear correlation coefficient of 0.97.


## 1. Introduction

The U.S. National Research Council (NRC 2009, 2010, 2012) has identified the need for a national network of ground-based boundary layer thermodynamic profilers to

fill a critical measurement gap that currently impedes the skill of weather prediction model forecasts. In particular, the variability of humidity in the lower troposphere is not adequately sampled at the mesoscale (NRC 2009). Improved water vapor measurements are also required for better understanding of the water and energy cycles (Wulfmeyer et al. 2015), which underpin a large number of operational and research efforts.

The radiosonde continues to be the de facto standard for water vapor profiling worldwide. These relatively

---

 Denotes content that is immediately available upon publication as open access.

---

Corresponding author: R. K. Newsom, rob.newsom@pnnl.gov

DOI: 10.1175/JTECH-D-18-0102.1

© 2020 American Meteorological Society. For information regarding reuse of this content and general copyright information, consult the [AMS Copyright Policy \(www.ametsoc.org/PUBSReuseLicenses\)](https://www.ametsoc.org/PUBSReuseLicenses).

simple and reliable instruments provide accurate in situ measurements of pressure, temperature and humidity as the sensor package ascends through the atmosphere. For practical purposes, radiosondes are only launched twice daily from most operational weather service sites. Furthermore, these sites are typically separated by hundreds of kilometers. Thus, the principal disadvantage with the existing radiosonde network is that they do not provide the temporal resolution and horizontal spatial resolution to adequately sample rapidly changing humidity fields, particularly in the atmospheric boundary layer (ABL).

Ground-based passive and active remote sensing techniques have improved temporal resolution and could potentially fill this measurement gap. The key to improving the spatial resolution is finding a reliable low-cost technology that can be deployed in large numbers.

Passive remote sensing techniques for humidity profiling include multichannel microwave radiometers (e.g., [Solheim et al. 1998](#); [Rose et al. 2005](#)) and infrared Fourier transform interferometers (e.g., [Knuteson et al. 2004a](#)). These passive systems, which are already commercially available, provide spectrally resolved measurements of downwelling radiance at the surface. Vertically resolved profiles of water vapor mixing ratio (WVMR) are obtained through inversion of a suitable radiative transfer model. The vertical resolution is primarily limited by the spectral information content of the observations; however, since the retrieval algorithm attempts to solve an ill-posed problem the dataset used to constrain the solution also has an impact on the vertical resolution. Infrared Fourier transform interferometers generally have a higher information content than microwave radiometers ([Löhnert et al. 2009](#); [Blumberg et al. 2015](#)), resulting in better vertical resolution, but the useful range is limited to a couple of kilometers (e.g., [Turner and Löhnert 2014](#)).

Active remote sensing techniques for humidity profiling include differential absorption and Raman lidar (RL). Raman lidars make use of weak inelastic scattering from atmospheric water vapor molecules to infer WVMR. Raman lidars have proven to be capable of producing accurate WVMR profiles with good vertical and temporal resolution. However, there are currently only a handful of these instruments that are operational worldwide ([Goldsmith et al. 1998](#); [Turner and Goldsmith 1999](#); [Turner et al. 2016](#); [Dinoev et al. 2013](#); [Reichardt et al. 2012](#)). Furthermore, these tend to be expensive research-grade instruments that require powerful (usually non-eye-safe) laser transmitters and large receiver apertures to detect the weak inelastic scattering. Another drawback is that Raman

lidars require independent ancillary observations for calibration, for example, from a radiosonde or microwave radiometer ([Whiteman et al. 1992](#); [Turner and Goldsmith 1999](#)). Additionally, some RLs exhibit some degree of residual overlap which can result in large biases in WVMR at low altitudes.

Differential absorption lidars (DIAL) produce range-resolved measurements of trace gas concentrations from the difference in attenuation observed between two closely spaced (in the spectral sense) laser lines. Since two laser lines are needed, the transmitter is more complex than a Raman lidar, but generally somewhat simpler on the receiver side. The smaller telescope and the availability of relatively inexpensive laser diodes in the near IR allows for the possibility of more compact and less expensive designs compared to the Raman lidar.

To address the need for inexpensive and reliable water vapor profiling, a number of groups have developed DIAL systems utilizing diode laser transmitters with low pulse energy and high pulse repetition rates. This includes the micropulse DIAL (MPD) developed at Montana State University and the National Center for Atmospheric Research ([Spuler et al. 2015](#); [Weckwerth et al. 2016](#)). The MPD makes use of the more traditional narrow-band approach in which the spectral width of the transmit laser is much narrower than the targeted absorption feature. Also, a group at Tokyo Metropolitan University has recently demonstrated a system utilizing narrow-band transmission combined with photoacoustic spectroscopy for wavelength locking ([Le Hoai et al. 2016](#)). One of the advantages of narrowband DIAL is its ability to make humidity measurements without the need for calibration. This requires that the laser be extremely stable and spectrally pure, which adds to the complexity of the design.

Various alternatives to the narrow-band approach have been proposed and/or demonstrated over the years. This includes techniques which use very broadband laser sources (spanning hundreds or even thousands of individual absorption lines) combined with either narrow-band detection as in the case of “BELINDA” ([Weitkamp 2005](#)), or spectrally resolved measurements of the backscatter return ([Povey et al. 1998](#); [South et al. 1998](#)).

In this study, we describe the performance of a prototype DIAL system, developed by Vaisala, that utilizes a broadband approach in which the laser spectrum spans several water vapor absorption features. We refer to this approach as broadband DIAL, or BB-DIAL. The performance of the Vaisala BB-DIAL system was previously evaluated during field campaigns in Germany, Finland ([Roininen and Mönkel 2017](#)), and Hong Kong

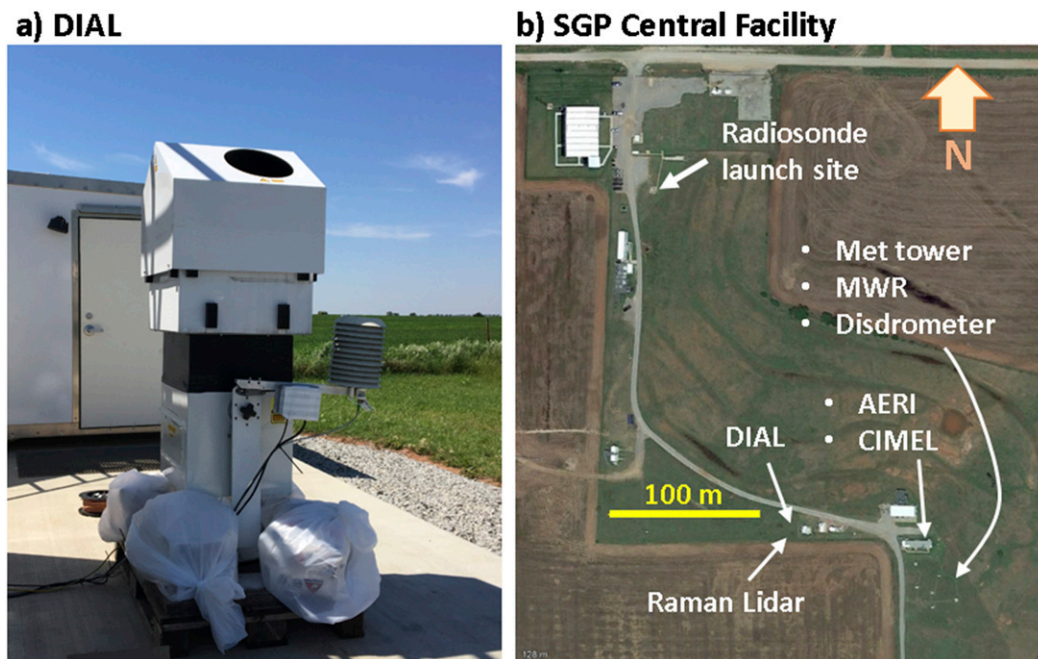


FIG. 1. (a) The Vaisala BB-DIAL, and (b) aerial view of the SGP central facility showing the locations of the BB-DIAL, RL, AERI, and radiosonde launch site.

(Münkel and Roininen 2017). The goal of this paper is to provide an overview of the design, and present the results of a comprehensive intercomparison with other collocated ground-based humidity profiling systems.

Evaluation of the Vaisala BB-DIAL system was conducted at the U.S. Department of Energy's Atmospheric Radiation Measurement (ARM) Southern Great Plains (SGP) site in north-central Oklahoma (Sisterson et al. 2016; 36.605°N, 97.486°W). This site contains a vast array of atmospheric and terrestrial measurement systems that are permanently deployed and continuously operated (Mather and Voyles 2013). For this study, we compare the height-resolved water vapor measurements from the BB-DIAL with those of a Raman lidar (RL), an Atmospheric Emitted Radiance Interferometer (AERI), and radiosondes. The evaluation was carried out over a period of 28 days from 15 May to 12 June 2017.

## 2. Field campaign and instrument descriptions

The area surrounding the SGP site is largely flat and is primarily open pasture and rangeland (Sisterson et al. 2016). Figure 1b shows the SGP site and the locations of the BB-DIAL, RL, AERI and the radiosonde launch site. The BB-DIAL was deployed within 5 m of the RL during the evaluation campaign. The BB-DIAL operated unattended and continuously for 28 days from 15 May until 12 June 2017.

The launch site for the radiosondes was located approximately 245 m NNW of the BB-DIAL and Raman lidars. Radiosondes are launched four times daily at the SGP site. The AERI is housed in a trailer located about 80 m east of the lidars. In addition to the BB-DIAL, RL, AERI and radiosondes, there are number of other supporting instruments used in the study. These include a 10-m meteorological tower, a two-channel microwave radiometer (MWR), and a disdrometer located in the southeast corner of Fig. 1b. The 10-m tower provided measurements of winds at 10 m and temperature and humidity at 2 m. The MWR (Cadeddu et al. 2013) provided measurements of precipitable water vapor (PWV), and the disdrometer provided rain-rate measurements. Additionally, a sun photometer (CIMEL) was collocated with the AERI. The CIMEL (Holben et al. 1998) provided measurements of aerosol optical depth (AOD) at 15 wavelengths ranging from 340 to 1640 nm.

Figure 2 summarizes the mean state of the atmospheric boundary layer during the field campaign. The PWV distribution (Fig. 2a), obtained from the MWR, shows that PWV values ranged from just above 1 cm to about 6 cm, with a maximum in distribution occurring at just over 3 cm. Profiles of median relative humidity and WVMR (Fig. 2b) from the radiosondes indicate moderately humid conditions, with surface relative humidity values varying between roughly 50% and 70%. The nighttime soundings (i.e., the 0530 UTC soundings)

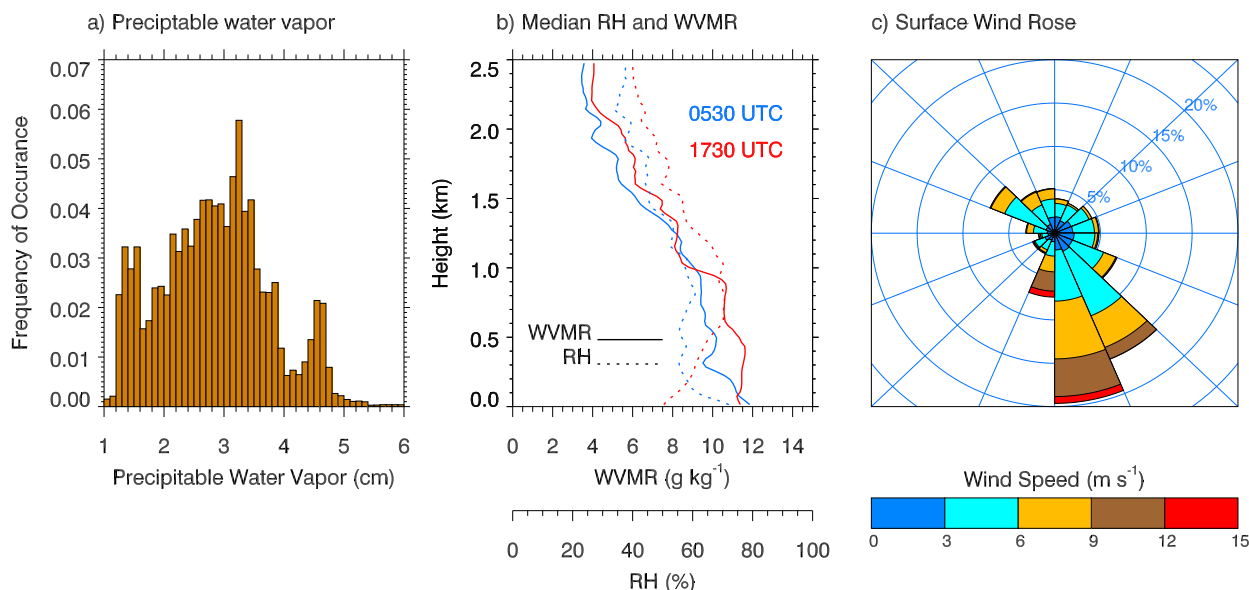


FIG. 2. Mean atmospheric conditions from 15 May through 12 Jun 2017 at the SGP central facility showing (a) the distribution of PWV from MWR data, (b) profiles of median WVMR (solid) and relative humidity (dashed) from nighttime soundings at 0530 UTC (blue) and from daytime soundings at 1730 UTC (red), and (c) the wind rose at 10 m from the surface meteorological station.

generally show smaller values of WVMR than the daytime soundings (i.e., the 1730 UTC soundings). The mean winds at 10 m AGL (Fig. 2c) were obtained from a surface meteorological station located roughly 100 m east-southeast of the BB-DIAL, as indicated in Fig. 1b. The prevailing winds during the field campaign were south-southeasterly, with wind directions between  $112^\circ$  and  $203^\circ$  occurring roughly 50% of the time. Southerly flows were also associated with the highest wind speeds. These southerly flows are also often responsible for transporting warm humid air up from the Gulf of Mexico.

Disdrometer measurements (Bartholomew 2016) at the SGP site indicate there were about 27 distinct rain events with measurable precipitation during the course of the field campaign. Four of these events had maximum precipitation rates between 1 and  $10 \text{ mm h}^{-1}$ , and five events had maximum precipitation rates greater than  $10 \text{ mm h}^{-1}$ . The five heaviest rain events occurred on 18, 19, 23, and 28 May and 4 June, with the highest rain rate ( $\sim 40 \text{ mm h}^{-1}$ ) observed on 19 May.

#### a. BB-DIAL

Technical specifications of the Vaisala BB-DIAL prototype are summarized in Table 1. The system, which is pictured in Fig. 1a, uses diode laser transmitters to produce pulsed laser radiation at two closely spaced wavelengths (910.6 and 911.0 nm) with an American National Standards Institute (ANSI) eye-safety classification of 1M. The design includes two vertically pointing measurement units placed side by side (note

that only one telescope can be seen in Fig. 1a, because the second telescope is on the other side). Each measurement unit incorporates a monostatic configuration, with a ceilometer-type telescope design (Dabberdt et al. 2016; Roininen and Munkel 2017). One unit is optimized for near-range measurement from 50 up to 400 m, and the other for far-range measurement from 300 up to 3000 m. Cross talk between the units is eliminated by alternating transmission through each unit for a period of 5 s. Within each 5-s period, measurements are made by alternating between the offline and online wavelengths; the current prototype measures each wavelength for a duration of 0.138 s using avalanche photodiode detectors in analog mode. Each measurement unit uses a single transmitter and a common optical path for the online and offline signals. This ensures that the receiver efficiencies and overlap functions for the online and offline signals are essentially identical.

The BB-DIAL temporally averages the online and offline return signals during each 5-s measurement cycle. In the vertical, return signals are averaged using Gaussian-like weighting functions in which the full-width-at-half-maximum (FWHM) increases with height, as shown in Fig. 3. The FWHM of the weighting functions varies from 10 m at the surface to 200 m at 1000 m AGL and 500 m at 3000 m AGL. This vertical averaging scheme helps to maintain consistent measurement quality as the SNR decreases with height.

The BB-DIAL system generates humidity profiles using temporal resolutions of 2 and 20 min. The 20-min

TABLE 1. Specifications for the Vaisala BB-DIAL prototype.

Laser eye-safety classification	1M
Dimensions	1900 mm × 700 mm × 700 mm
Weight	130 kg
Averaging time/reporting interval	20 min/2 min
Max range	3000 m reported
Range resolution	100–500 m (see Fig. 3)
Average power per unit	44 mW
Laser type	Laser diode
Pulse energy	5.5 μJ
Pulse peak power	25 W
FWHM pulse width	220 ns (33 m)
Pulse repetition rate	8 kHz
Wavelength (online/offline)	911.0 nm/910.6 nm
FWHM spectral width (near/far range)	0.19 nm/0.17 nm
Telescopes	Lens telescope; coaxial transmit/receive (TX/RX) beams
Telescope diameter (near/far range)	150 mm/280 mm
Receiver detector	Avalanche photodiode (APD)
Receiver bandwidth	3 MHz (−3 dB)

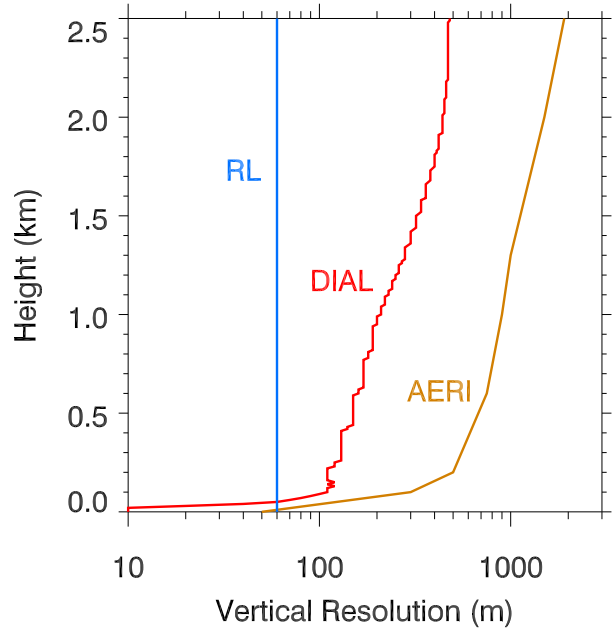


FIG. 3. Height dependence of the vertical resolution for the RL (blue), BB-DIAL (red), and AERI (brown).

data represent the final output, whereas the 2-min data are only used internally to estimate the uncertainty in the 20-min data. For both resolutions, the 5-s returns are averaged over the appropriate time interval (2 or 20 min), and the near- and far-range humidity profiles are then retrieved from the ratio of the average online to average offline returns. The near- and far-range humidity profiles are then merged into a single humidity profile using a weighted average over the height range from 300 to 400 m. The weights vary linearly across this range such that the result is entirely from the near-range unit below 300 m, and entirely from the far-range unit above 400 m.

The final humidity profiles are computed using a 20-min sliding average of the 5-s online and offline signal returns, with humidity profiles reported every two minutes. For this study, the results are reported in units of water vapor mixing ratio to allow easy comparison with the radiosondes and the Raman lidar. The BB-DIAL also generates estimates of uncertainty and maximum detection range. Uncertainty estimates are obtained from the standard deviation

of the 2-min data over the 20-min averaging period. The maximum detection range, which can be used to identify and reject poor quality data, is determined from the statistics of the 5-s signal ratio over the 20-min averaging period.

The BB-DIAL uses a broadband approach in which the spectrum of the laser output overlaps multiple water vapor absorption lines, as shown in Fig. 4. The offline laser is placed at 910.6 nm in a region of the spectrum with very low water vapor absorption, and the online laser is placed in a region of the spectrum with much stronger water vapor absorption at 911.0 nm. In Fig. 4, the online and offline laser spectra are modeled using Gaussian functions. The Gaussian provides an accurate approximation to the average spectrum of the diode laser transmitter.

Equation (24) in Wulfmeyer et al. (2015) gives a general expression for the range dependence of the backscattered power. This expression, which takes into account the extended laser spectrum, is given by

$$P_{\nu_x}(z) = P_{\nu_x}(0) \frac{\eta_{\nu_x}}{z^2} O(z) T_{\text{air},\nu_x}^2(z) \times \left\{ \beta_{p,\nu_x}(z) \int_{-\infty}^{\infty} S_x(\nu - \nu_x) T_{\text{WV}}^2(\nu, z) F(\nu) d\nu + \beta_{m,\nu_x}(z) \int_{-\infty}^{\infty} S_x(\nu - \nu_x) T_{\text{WV}}^2(\nu, z) \text{DB}(\nu, z) F(\nu) d\nu \right\} + P_{B,\nu_x}, \quad (1)$$

where  $\nu_x$  denotes the center frequency of the online ( $\nu_{\text{on}}$ ) or the offline ( $\nu_{\text{off}}$ ) laser;  $P_{\nu_x}(0)$  is the peak power of the transmitted beam;  $\eta_{\nu_x}$  is a parameter that depends

on the transceiver optical efficiency, pulse width, and telescope area;  $O(z)$  is the overlap function;  $T_{\text{air},\nu_x}(z)$  is the one-way transmission due to particulate and

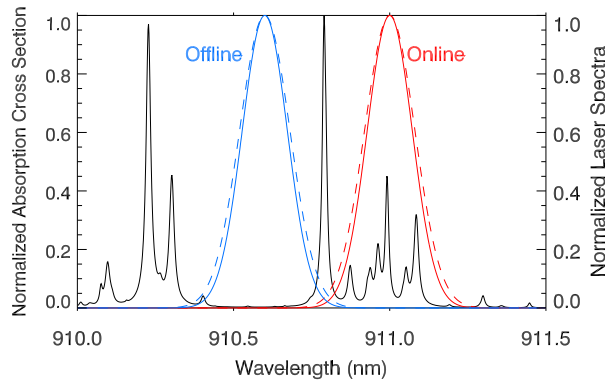


FIG. 4. Normalized water vapor absorption cross section at 296 K and 1 atm (black). The normalized laser spectra for the far-field (solid) and near-field (dashed) are shown in red for the online laser spectra and blue for the offline laser spectra.

molecular scattering (from  $N_2$  and  $O_2$ );  $\beta_{p,\nu_x}$  is the particulate backscatter coefficient;  $\beta_{m,\nu_x}$  is the molecular backscatter coefficient;  $S_x(\nu)$  is the normalized laser spectrum;  $F(\nu)$  is the receiver transmission function;  $DB(\nu, z)$  is the Doppler broadening of the molecular backscatter; and  $P_{B,\nu_x}$  is the background power level due to ambient and solar radiation and detector dark current. The  $T_{WV}(\nu, z)$  is the one-way transmission due to water vapor absorption, and is given by

$$T_{WV}(\nu, z) = \exp\left(-\int_0^z N(z)\gamma(\nu, z) dz\right), \quad (2)$$

where  $N(z)$  and  $\gamma(\nu, z)$  are the  $H_2O$  molecular number density and absorption cross section, respectively.

A general broadband DIAL equation is obtained from the ratio of the background-subtracted and pulse normalized online and offline signals. Taking the ratio results in near complete cancellation of  $\eta_{\nu_x}$ ,  $O(z)$ , and the atmospheric transmission terms  $T_{air,\nu_x}(z)$  because of the closeness of the online and offline frequencies. For operation near 900 nm in the ABL, the aerosol backscatter term in Eq. (1) dominates the return signal so that the molecular backscatter term can be neglected. Also, the receiver transmission function,  $F(\nu)$ , is spectrally flat over the wavenumber band that includes the online and offline laser spectra. The ratio of the online-to-offline signals then becomes

$$\frac{P'_{\nu_{on}}}{P'_{\nu_{off}}} \approx \frac{\int_{-\infty}^{\infty} S_{on}(\nu - \nu_{on})T_{WV}^2(\nu, z) d\nu}{\int_{-\infty}^{\infty} S_{off}(\nu - \nu_{off})T_{WV}^2(\nu, z) d\nu}, \quad (3)$$

where

$$P'_{\nu_x}(z) = [P_{\nu_x}(z) - P_{B,\nu_x}]/P_{x0} \quad (4)$$

accounts for corrections to the signal magnitude and offset. Also, in Eq. (3) we have assumed  $\beta_{p,\nu_{on}}/\beta_{p,\nu_{off}} \approx 1$  because of the closeness of the online and offline frequencies.

Equation (3) forms the basis for the humidity retrieval algorithm implemented by the Vaisala BB-DIAL. Information about the vertical profile of humidity is contained in  $T_{WV}$  through its dependence on  $N(z)$ . Computation of the right hand side of Eq. (3) requires knowledge of the online and offline laser spectra, the water vapor absorption cross section  $\gamma(\nu, z)$ , and the  $H_2O$  molecular number density  $N(z)$ .

Unlike narrowband DIAL, it is not possible to obtain a closed-form solution for  $N(z)$  from Eq. (3). However, a unique solution for  $N(z)$  can still be obtained through the use of an appropriate inversion method (Wulfmeyer et al. 2015). Although the precise details of this solution method are considered to be proprietary by Vaisala, the general idea is to find the optimal value of  $N(z)$  at each height level such that Eq. (3) is satisfied. This is equivalent to finding the minimum of

$$\text{cost}(z) = \left[ \frac{P'_{\nu_{on}} - \int_{-\infty}^{\infty} S_{on}(\nu - \nu_{on})T_{WV}^2(\nu, z) d\nu}{P'_{\nu_{off}} - \int_{-\infty}^{\infty} S_{off}(\nu - \nu_{off})T_{WV}^2(\nu, z) d\nu} \right]^2 \quad (5)$$

with respect to  $N(z)$ . The retrieval process starts at ground level using surface measurements of humidity, temperature and pressure, and then progresses upward range gate by range gate, in a manner similar to the method used by South et al. (1998). Figure 5 shows an example of the behavior of how the Eq. (5) varies with  $N$ . For this example, the spectral parameters of the water vapor absorption cross section were determined using a radiosonde profile acquired under convective condition at 1730 UTC 6 June 2017. The cost function was evaluated by perturbing the water vapor number density from its actual observed value, while keeping all other parameters constant. Figure 5 indicates that the cost function exhibits a well-defined global minimum at the observed value of  $N$ .

The spectral parameters of the water vapor absorption cross section (line positions and widths) are temperature and pressure dependent. For this reason, the BB-DIAL system incorporates sensors that measure surface temperature, pressure, and relative humidity. The temperature and pressure measurements are vertically extrapolated assuming the International Organization for Standardization

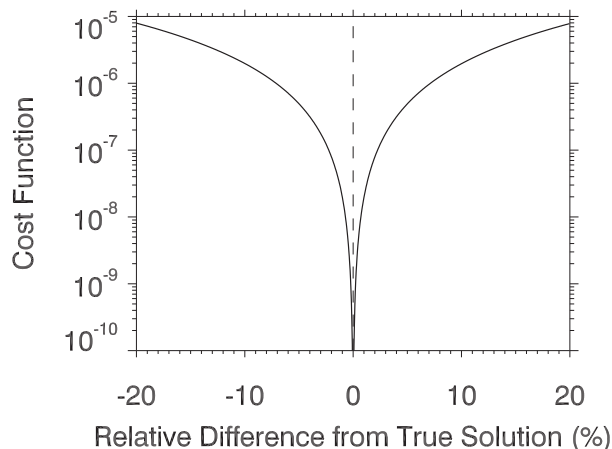


FIG. 5. The cost function [Eq. (5)] vs the relative difference between the true water vapor number density and the perturbed value. The relative difference is positive if the perturbed value is greater than the true value. The cost function was evaluated at 500 m AGL using a radiosonde profile acquired at 1730 UTC 6 Jun 2017.

(ISO) 2533–1975 standard atmospheric model with a vertical temperature gradient of  $-0.0065 \text{ K m}^{-1}$ . The extrapolated profiles are then used to estimate the positions and widths of the water vapor absorption lines from the “HITRAN” database (Rothman et al. 2009). The surface humidity measurements are also used to establish the humidity value in the lowest altitude bin of the retrieval, where the transmitter/receiver overlap is not sufficient for good quality measurements. For the current prototype, this occurs for altitudes below 50 m.

The use of the standard atmospheric model to establish the spectral parameters of the water vapor absorption cross section is expected to introduce some error. To estimate this error, we used the standard atmospheric model to define the spectral line widths and positions, and then retrieved the water vapor concentration by minimizing Eq. (5). For this analysis we used a radiosonde profile acquired at 1730 UTC 7 June 2017 to define the true solution and to establish the surface temperature and pressure values for the standard atmospheric model. Figure 6a shows the differences in the temperature and pressure profiles between the radiosonde observations and the standard atmospheric model. Although these differences can be very large, the relative error in the retrieved number density is relatively small, as shown in Fig. 6b. In this example, the error increases with height from zero at the surface to about  $-0.2\%$  at 3 km AGL. This indicates that the retrieved water vapor concentrations are not very sensitive to the temperature and pressure profiles used to establish the spectral parameters.

The retrieval algorithm requires accurate specification of the online and offline laser spectra. For the current BB-DIAL prototype, the laser spectra for the far- and near-range units were measured in the laboratory using an Ando AQ 6317 optical spectrum analyzer with optical fiber input. The spectrum analyzer was able to provide very accurate measurements of the center wavelengths. However, uncertainties in the spectral resolution of the spectrum analyzer resulted in uncertainty in the spectral width estimates, which can lead to bias in the humidity retrievals. We note that the retrieval is more sensitive to uncertainty in the spectral width in high humidity conditions. To reduce this uncertainty, collocated radiosonde data collected during the current field campaign and two other campaigns in 2017 (Roininen and Munkel 2017; Munkel and Roininen 2017) were used. We compared WVMR from the radiosonde and the BB-DIAL retrievals over the whole dataset while varying the near- and far-range spectral widths until a good agreement was obtained. It is important to note that the same spectral widths (and center wavelengths) were used to process data from the current field campaign, as well as the two other campaigns in 2017.

#### b. Raman lidar

The ARM program has operated a Raman lidar (RL) at the SGP central facility since 1996 (Turner et al. 2016). This system incorporates a monostatic design utilizing a 61 cm telescope, and transmits pulses of laser energy at a wavelength of 355 nm. The pulse energy, pulse duration, and repetition frequency are 300 mJ, 5 ns, and 30 Hz, respectively (Goldsmith et al. 1998). The design incorporates nine detection channels that are split between wide and narrow fields of view (FOV) (2.0 and 0.3 mrad, respectively). The wide FOV includes one (unpolarized) elastic channel at 355 nm, a water vapor channel at 407.5 nm, and a nitrogen channel at 387 nm. The narrow FOV includes one copolarization elastic channel, one depolarization elastic channel, one water vapor channel, one nitrogen channel, and two rotational Raman channels for temperature measurement (Newsom et al. 2013; Turner et al. 2016). The detection electronics provide simultaneous measurements of analog voltage and photon counts. The photon counting data are corrected for nonlinear system dead-time effects, and then combined with the analog voltage data to provide backscatter profiles at 7.5-m, 10-s resolution (Newsom et al. 2009).

Taking the ratio of the lidar equations for the water vapor and nitrogen channels yields the following result:

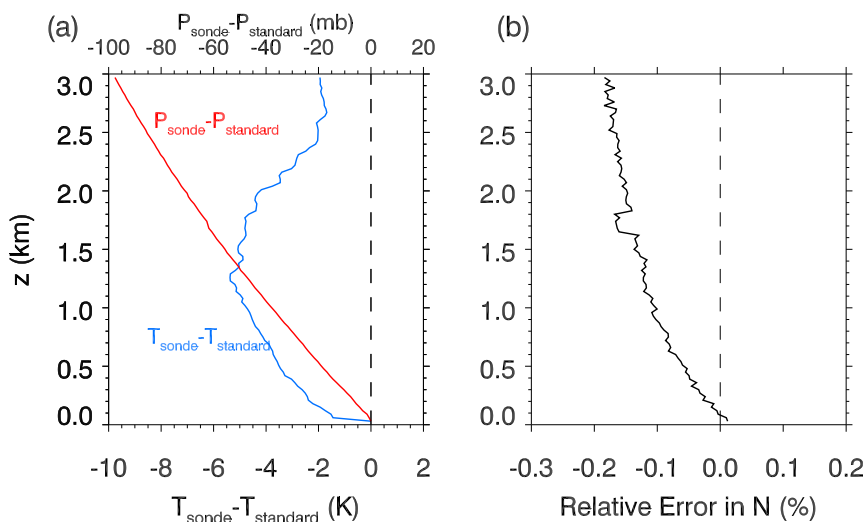


FIG. 6. Examples of (a) the difference between radiosonde measurements of temperature and pressure and those predicted by the ISO 2533–1975 standard atmospheric model and (b) the relative error between the true and retrieved water vapor number density due to the use of the standard atmospheric model in establishing spectral parameters in the absorption cross section. The relative error in (b) is positive when the retrieved number density is greater than the true (observed) number density. This example uses a radiosonde profile acquired under convective conditions at 1730 UTC 7 Jun 2017.

$$\text{WVMR}(z) = kO(z) \left[ \frac{P_{\text{H}_2\text{O}}(z)}{P_{\text{N}_2}(z)} \right] \left[ \frac{T_{\text{mol}}(\lambda_{\text{N}_2}, z)}{T_{\text{mol}}(\lambda_{\text{H}_2\text{O}}, z)} \right] \times \left[ \frac{T_{\text{aer}}(\lambda_{\text{N}_2}, z)}{T_{\text{aer}}(\lambda_{\text{H}_2\text{O}}, z)} \right], \quad (6)$$

where  $k$  is a calibration constant,  $O(z)$  is the ratio of the nitrogen-to-water channel overlap functions,  $P_x(z)$  is the observed background-subtracted backscatter signal from channel  $x$ ,  $T_{\text{mol}}(\lambda_x, z)$  is the molecular transmission at wavelength  $\lambda_x$ , and  $T_{\text{aer}}(\lambda_x, z)$  is the aerosol transmission at wavelength  $\lambda_x$ .

The molecular transmissions  $T_{\text{mol}}(\lambda_x, z)$  are readily calculated using semiempirical formulas from Bucholtz (1995) for the Rayleigh cross section, together with height-resolved molecular number density estimates computed from radiosonde data. On the other hand, estimating the aerosol transmissions requires height-resolved estimates of aerosol extinction, which can in principle be computed from the any of the inelastic signals, for example, the nitrogen signal (Ansmann et al. 1990). However, the retrieved extinction profiles are typically quite noisy, and strongly affected by overlap. As a result, the aerosol transmission correction can occasionally introduce undesired artifacts in the retrieved WVMR. For this reason, we assume that  $T_{\text{aer}}(\lambda_{\text{N}_2}, z)/T_{\text{aer}}(\lambda_{\text{H}_2\text{O}}, z) \approx 1$ , which is a reasonable

assumption when the AOD is small. From CIMEL measurements we note that the median AOD at 380 nm during the field campaign was 0.18, with AOD values below 0.5 occurring 94% of the time. When AOD = 0.2, for example, the expected error is less than 3% for altitudes at and below 2 km (Whiteman 2003; Foth et al. 2015).

We refer to the product of the calibration coefficient with the overlap function,  $kO(z)$ , as the calibration profile. When processing the RL data, a single calibration profile is determined and used for a given 24-h period by shifting and scaling a so-called “baseline” calibration profile to achieve a best fit with the radiosonde WVMR observations during that 24-h period. The baseline calibration is determined from the median ratio of the radiosonde WVMR to the transmission-corrected signal ratio,  $P_{\text{H}_2\text{O}}T_{\text{mol}}(\lambda_{\text{N}_2})/P_{\text{N}_2}T_{\text{mol}}(\lambda_{\text{H}_2\text{O}})$ , over the course of the entire field campaign. We note that the signal ratio becomes increasingly unstable as the height approaches zero, making it difficult to accurately calibrate the RL for altitudes below roughly 200–300 m.

The calibration procedure is performed separately for both the WFOV and the NFOV. The calibrated NFOV and WFOV WVMRs are then merged into a single profile. The merged field is a weighted average of the WFOV with the NFOV. The weights vary linearly with height such that the merged field is 100% WFOV at the surface, and 100% NFOV at 1.2 km AGL and above. For this study, the RL WVMR data were processed using a temporal and vertical averaging interval



of 10 min and 60 m, respectively, with no oversampling in time or height. Thus, each time and range bin represents independent WVMR measurements. Also, estimates of the uncertainty in the WVMR are obtained by propagating the effects of shot noise through the calculations. The relative uncertainty is then used as a quality control parameter. For this study, measurements that exceed a relative uncertainty of 25% are not used when evaluating differences or correlations between instruments.

### c. AERI

The Atmospheric Emitted Radiance Interferometer is a ground-based Fourier transform spectrometer that measures the downwelling sky spectral radiance immediately above the instrument (Knuteson et al. 2004a,b; Feltz et al. 2003). AERI's FOV is  $1.3^\circ$ , centered on zenith, and radiances are measured in the range from 3 to  $19.2\ \mu\text{m}$  at a resolution of better than  $1.0\ \text{cm}^{-1}$ . Radiances are calibrated to within an uncertainty of 1% of the ambient radiance (Knuteson et al. 2004b). A calibrated sky radiance spectrum is produced every 20 s in rapid sampling mode, and a filter is applied to reduce the random noise level (Turner et al. 2006).

The retrieval of thermodynamic profiles from the AERI radiance observations is an ill-posed problem. To address this, the AERIOe algorithm was developed to perform physical-iterative retrievals that are constrained by an a priori dataset (Turner and Löhnert 2014). The method starts with a first guess thermodynamic profile, which is typically the mean a priori profile, which is input into the Line-By-Line Radiative Transfer Model (LBLRTM) (Mlawer et al. 2012). The LBLRTM has been well-validated against spectral observations (Mlawer and Turner 2016). The simulated AERI observation is compared to the true observation; if the difference is larger than the measurement uncertainty then the Jacobian (which is also computed using the LBLRTM) is used to derive an improved first guess and the process is repeated. A monthly climatology of approximately 2000 radiosondes launched at the ARM site from 1992 to 2010 is used as the a priori dataset, which primarily provides the level-to-level covariance of temperature and humidity that serves as the constraint on the solution (i.e., retrieved profile). The concurrent radiosonde data collected at the SGP site are not used in the AERIOe retrieval in any way. The vertical resolution of the AERIOe retrievals (Fig. 3), which is also produced directly by the algorithm, degrades with altitude due to the spreading of weighting functions and the covariance of the a priori. Additional information from the surface meteorological observations and temperature and water vapor profiles from the Rapid Refresh numerical

weather prediction model (Benjamin et al. 2016) above 4 km were included as additional input into the AERIOe retrieval to better constrain the solution (Turner and Blumberg 2019). Because the AERIOe is a 1D variational retrieval algorithm, instrument uncertainties and the sensitivity of the LBLRTM are propagated to provide a full error characterization of the solution (Turner and Löhnert 2014; Turner and Blumberg 2019). The AERIOe is able to provide retrieved profiles at the maximum temporal resolution of the AERI (i.e., 30 s), but for this work 5-min profiles were produced.

### d. Radiosondes

Radiosondes are launched from the SGP central facility four times daily. The nominal launch times are 0530, 1130, 1730, and 2330 UTC corresponding to 0030, 0630, 1230, and 1830 central daylight time, respectively. During the evaluation period, the ARM program was using the RS92 radiosonde at SGP (ARM switched to the RS41 in the autumn of 2017). Both the RS92 and RS41 radiosondes are manufactured by Vaisala (Steinbrecht et al. 2008). The radiosondes provide height-resolved measurements of temperature, pressure and humidity at a sampling rate of 1 Hz. With a nominal ascent rate of  $\sim 5\ \text{m s}^{-1}$ , this results in a vertical resolution of roughly 5 m.

The RS92 radiosonde measurements of humidity have a well-documented dry bias that is due to the exposure of the RH sensor to solar radiation (Wang et al. 2013; Dzambo et al. 2016; Miloshevich et al. 2009; Cady-Pereira et al. 2008). A number of schemes have been developed to correct for this solar radiation dry bias (SRDB). In this study, we use the Wang et al. (2013) algorithm to correct the RS92 measurements of RH and temperature. This algorithm is effective at reducing the dry bias, but it leaves a small residual bias that increases with increasing PWV (Dzambo et al. 2016). Thus, the SRDB-corrected humidity profiles are also scaled in order to match the PWV measurements retrieved from a MWR at the SGP central facility. This scaling also helps to reduce biases due to calibration uncertainties in the radiosondes (Turner et al. 2003). Throughout this paper we refer to the original RS92 data as “uncorrected” and the profiles that had both the SRDB-correction and the PWV-scaling as “corrected.” Comparisons are presented using both the corrected and uncorrected radiosonde data.

## 3. Results

The time–height cross sections of WVMR shown in Fig. 7 indicate good qualitative agreement between the radiosonde, BB-DIAL, RL, and AERI. The BB-DIAL measurements have been screened to reject measurements

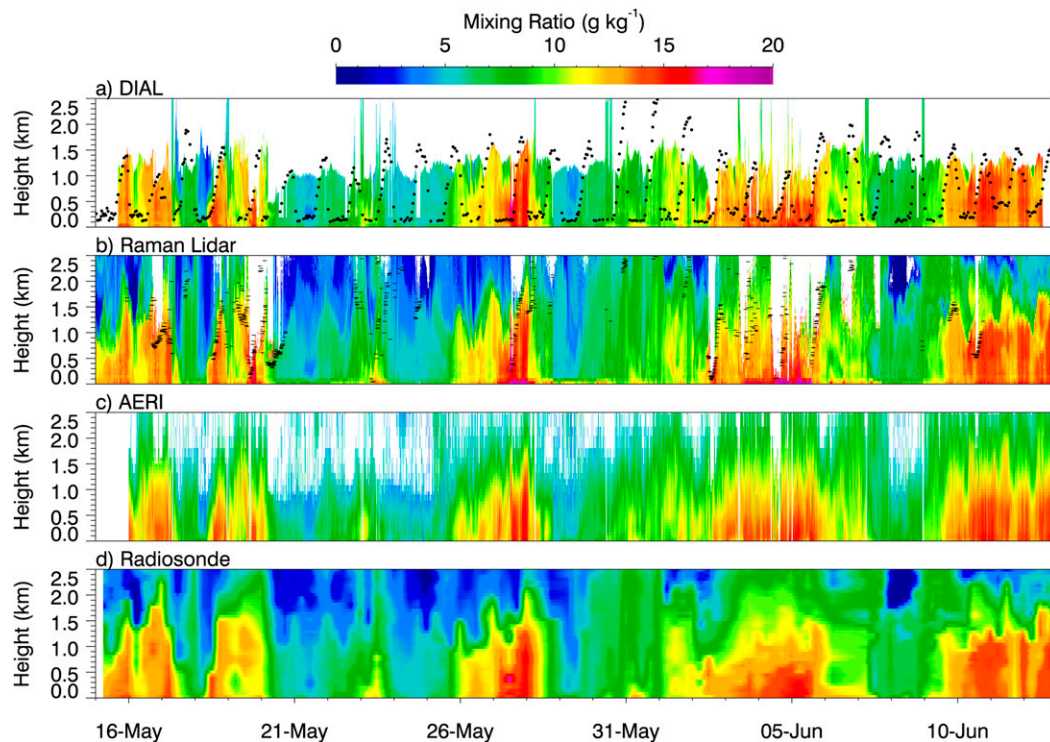


FIG. 7. Time–height cross sections of WVMR as observed by the (a) BB-DIAL, (b) RL, (c) AERI, and (d) corrected radiosondes. The BB-DIAL data were filtered to remove values above the maximum detection height. Similarly, the RL and AERI data were filtered to remove measurements with relative errors exceeding 25%. Also shown are estimates of the mixed layer height (black dots) in (a) and estimates of the cloud-base height (black dashes) in (b).

above the maximum detection height. Similarly, the Raman lidar and AERI data have been screened to reject values with relative errors exceeding 25%. The radiosonde data have been interpolated between sounding times to obtain a continuous time series for display purposes. The temporal resolutions are 20 min for the BB-DIAL (oversampled at 2-min intervals), 10 min for the RL, and 5 min for the AERI. The radiosonde, on the other hand represents a snapshot of the atmosphere taken once every 6 h. Additionally, Fig. 7b shows estimates of cloud-base height (black dashes) as computed from the RL's elastic channel data, and Fig. 7a shows estimates of the mixed layer height  $z_i$  computed from vertical velocity variance measurements obtained from a vertically staring Doppler lidar collocated with the RL (Berg et al. 2017).

An important performance metric for field instruments designed to operate autonomously is the percentage of time that the instrument produces valid measurements, that is, the data availability (DA). Figure 8 shows the DA as a function of height for the BB-DIAL, Raman lidar, and AERI. The DA is computed by adding the number of valid samples at a fixed height and dividing by the total number of time samples that were possible over the duration of the field

campaign. The DA thus represents the percent of time that the instrument was working and producing valid estimates. For the BB-DIAL, a sample is deemed valid if it falls below the maximum detection range as defined in the BB-DIAL output data files. For the RL and the AERI, valid samples are those for which the relative error is less than 25%. Note that low-level liquid-water clouds attenuate both lidars and are generally opaque for the AERI, and thus none of the remote sensors used in this study are able to profile through or above these types of clouds.

Figure 8 shows that the BB-DIAL's DA is nearly 100% below about 200 m AGL. It falls abruptly to about 95% at 200 m and decreases gradually to about 90% at 800 m. Above 800 m the DA drops steeply to less than 10% above 1500 m. The AERI DA is roughly constant with height below about 800 m at just over 90%. Above 800 m the AERI DA decreases in a linear fashion to about 30% at 2500 m AGL. By contrast, the RL DA experiences a relatively gradual decrease with height from just below 100% at 200 m to about 70% at 2500 m.

The percent coverage of the atmospheric boundary layer by the BB-DIAL was found to be 83%. This was determined from the ratio of the number of time and

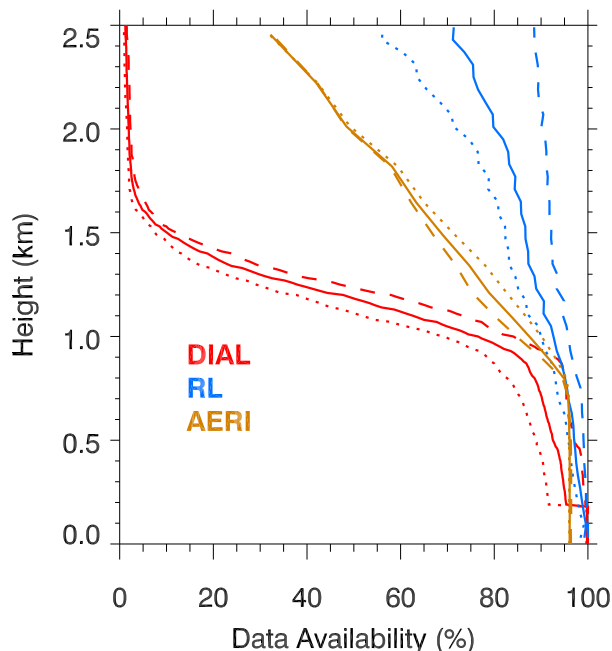


FIG. 8. Profiles of data availability (DA) for the period from 15 May 2017 through 12 Jun 2017 for the BB-DIAL (red), RL (blue), and AERI (brown). The dotted and dashed lines show the daytime and nighttime DAs, respectively, and the solid lines show the DAs for all times.

height bins with valid measurements at or below  $z_i$  to the total number of bins at or below  $z_i$  over the course of the field campaign. From Fig. 7a it is clear that the majority of missing values below  $z_i$  occur during the afternoon when the boundary layer is at or near its maximum depth. The mean daily maximum  $z_i$  during the field campaign was found to be 1620 m. At this height the BB-DIAL DA is less than 5%.

We note that AERI's maximum DA is smaller than the RL and the BB-DIAL. This is because AERI's hatch is programmed close in both heavy and light precipitation in order to protect its foreoptics (Knuteson et al. 2004a), while the BB-DIAL and the RL continue profiling. In the case of light precipitation, the BB-DIAL and the RL continue to produce valid measurements, albeit with reduced range.

The DAs for nighttime and daytime operation are also shown in Fig. 8. The BB-DIAL and RL both show more sensitivity to solar background radiation than does AERI, as indicated by the differences in DA from night to day. The RL in particular shows the largest changes from night to day. This is expected given the sensitivity of the RL's water vapor and nitrogen channels to solar radiation.

Figure 9 shows time–height cross sections of WVMR from the BB-DIAL, RL, and AERI for a 2-day period

from 0000 UTC 27 May to 0000 UTC 29 May. This period experienced the highest observed WVMRs during the entire field campaign. The largest WVMRs occurred shortly after sunrise on 27 May, near 1200 UTC. The increase in the WVMR leading up to that time was associated with a gradual shift in the wind direction from easterly to southerly. The WVMRs remained relatively high, with light and variable surface winds during the daytime period of 27 May. Light precipitation was observed between 0200 and 0300 UTC 28 May, and a much heavier precipitation event occurred later between 0500 and 0700 UTC with a maximum rain rate of about  $30 \text{ mm h}^{-1}$  at about 0530 UTC (during this period the AERI's hatch was closed). Then during the evening transition early on 28 May the wind speed increased and the wind direction shifted to northerly. This was associated with a marked decrease in the WVMR. Winds remained northerly for the rest of 28 May.

A direct comparison between the corrected radiosonde, BB-DIAL, RL, and AERI WVMR profiles is shown in Fig. 10. These examples are taken from four sounding times on 27 and 28 May 2017, as indicated by the dashed lines in Fig. 9. The RL and the BB-DIAL appear to show the best overall agreement with the radiosonde. By contrast, the AERI profiles are much smoother (due to its vertical resolution; Fig. 3), and have difficulty representing sharp changes with height.

For the RL, the accuracy of the WVMR in the lowest part of the atmosphere is often limited by errors in the estimation of the overlap function, particularly below roughly 500 m. Figure 10 shows that the RL consistently overestimates the WVMR in its lowest range gate. Also, the RL shows an underestimation of WVMR between roughly 100 and 400 m AGL in Figs. 10a and 10b that is likely due to uncompensated overlap. By contrast, BB-DIAL profiles show no obvious signs of overlap effects.

To quantify the differences in WVMR measurements between the various instruments we examine the mean difference or bias, the standard deviation of the difference stDev, the Pearson linear correlation coefficient Corr, and the slope and the offset from a linear regression analysis. For this analysis the observations must be defined on a common time and height grid. We take the BB-DIAL, RL, and AERI profiles that occur closest in time to a given radiosonde launch. In the vertical, we use the RL height grid as the common grid, and the other instruments are either interpolated or averaged to this height grid. In the case of the BB-DIAL and the AERI, their true vertical resolutions are, for the most part, coarser than the 60-m resolution of the RL. In that case, the BB-DIAL and AERI observations are linearly interpolated to the height grid of the RL. By contrast,

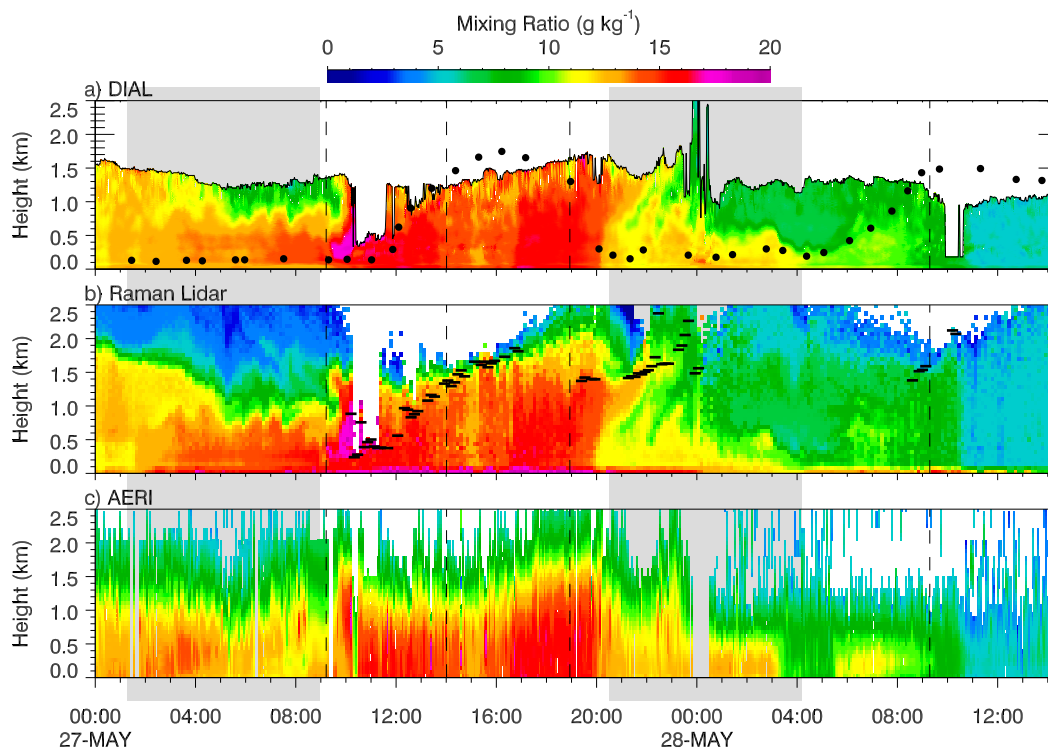


FIG. 9. Time–height cross sections of WVMR for 27 and 28 May 2017 showing (a) the BB-DIAL, its maximum detection height (solid black line), and estimates of the mixed layer height (solid black dots), (b) the RL WVMR and cloud-base height (black dashes), and (c) the AERI WVMR. Nighttime periods are indicated by the light-gray shading. The dashed vertical lines indicate radiosonde launch times. The BB-DIAL data were filtered to remove values above the maximum detection height. Similarly, the RL and AERI data were filtered to remove measurements with relative errors exceeding 25%. Times are shown in UTC.

the vertical resolution of the radiosonde data is typically much finer than the RL resolution. In that case, the radiosonde data are averaged within each range gate of the RL.

In our analysis we distinguish between two-way and four-way intercomparisons. In a four-way intercomparison, statistics between any two instruments are computed using only those time and height bins containing valid measurements from all four instruments. This approach ensures that the BB-DIAL, RL, and AERI are evaluated under exactly the same meteorological conditions. In a two-way intercomparison, statistics between any two instruments are computed completely independent of the other instruments.

Profiles of the median difference and the correlation coefficient between the corrected radiosonde and the other instruments are shown in Fig. 11. For these comparisons, we used a four-way intercomparison, and a maximum height of 1500 m since there are relatively few valid BB-DIAL measurements above this height. The median difference between the BB-DIAL and the corrected radiosonde (Fig. 11a) varies between roughly  $\pm 0.3 \text{ g kg}^{-1}$  and does not show any significant trend with

height. The correlation between the BB-DIAL and the radiosonde remains above 0.95 for heights below about 800 m. It then decreases gradually to roughly 0.9 at 1500 m AGL.

The median difference between the RL and the corrected radiosonde (Fig. 11b) remains close to zero for the most part with the exception of the lowest range gate, which is strongly affected by incomplete overlap between the transmitted beam and receiver FOV. The spread in the difference shows a decreasing trend with height (below 1500 m AGL). By contrast, the spread in the BB-DIAL measurements tends to increase with height. The RL correlation profile remains fairly constant with height for the most part. Not surprisingly, the worst correlations occur in the lowest two range gates. Another minimum in the correlation occurs at an altitude of about 1100 m, which may be related to the merging of the WFOV and NFOV WVMRs, as described in section 2b.

The median difference between the AERI and the radiosonde (Fig. 11c) exhibits a fairly substantial oscillation with height, with values ranging from roughly  $-0.6 \text{ g kg}^{-1}$  at 870 m AGL to about  $0.3 \text{ g kg}^{-1}$  at 270 m AGL. There

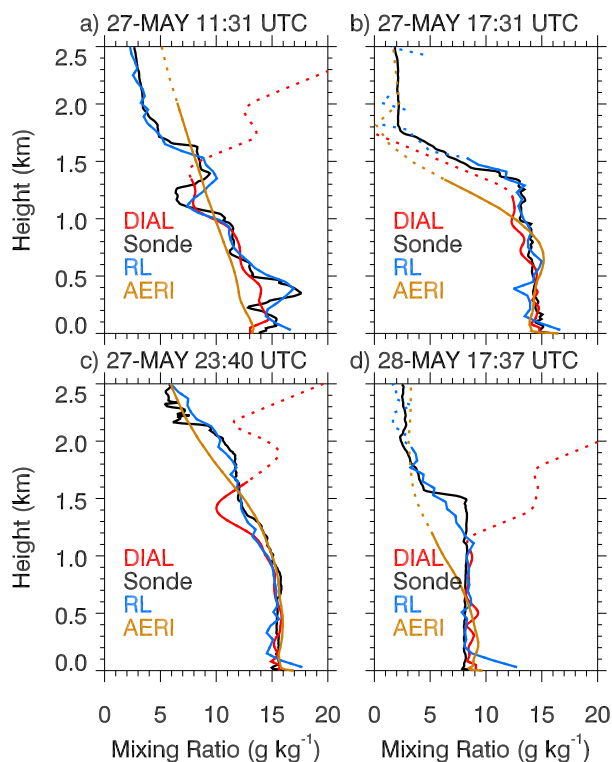


FIG. 10. Profiles of WVMR from the BB-DIAL (red), RL (blue), corrected radiosonde (black), and AERI (brown) at four sounding times, as indicated in each panel. Dotted lines indicate those portions of the profiles that do not pass the quality control requirements. For the BB-DIAL this includes those samples that occur above the maximum detection range. For the RL and the AERI this includes those samples whose relative uncertainties exceed 25%. Here, (b) and (d) both correspond to midday and (a) and (c) correspond to morning and evening transition periods, respectively.

is a distinct wet bias between about 50 and 500 m, and there is a distinct dry bias from about 500 to 1300 m. The spreads in the differences are also considerably larger than either the BB-DIAL or the RL. The correlation coefficient is approximately constant ( $\sim 0.95$ ) with height up to about 700 m. It then decreases to about 0.79 at 1500 m AGL.

Table 2 presents a summary of the statistics for the four-way intercomparisons between the radiosonde and the BB-DIAL, RL, and AERI. Here the statistics are computed over both time and height (below 1.5 km) and include the mean difference or bias, stDev, Corr, the mean percent difference (as defined by Weckwerth et al. 2016), and the slope and the offset from linear regression analyses.

Table 2 shows that biases for all three instruments are very small, with absolute values ranging from  $-0.01 \text{ g kg}^{-1}$  for the BB-DIAL to  $0.23 \text{ g kg}^{-1}$  for the AERI. The BB-DIAL and the RL show the lowest degree

of scatter with standard deviations of  $0.65$  and  $0.74 \text{ g kg}^{-1}$ , respectively. The AERI exhibits substantially more scatter with a standard deviation of  $1.23 \text{ g kg}^{-1}$ . The RL and the BB-DIAL show the best correlations at  $0.97$  and  $0.98$ , respectively. The AERI exhibits a smaller correlation of  $0.92$ . Linear regression analysis shows that the RL exhibits the best agreement with the radiosonde in terms of the slope and offset of the regression line. The slope of the regression line for the AERI–radiosonde comparison shows the largest departure from 1.

In Table 2 we observe that the BB-DIAL has the lowest mean percent difference at about 0.4%. Although this result is quite good, it is important to point out that the mean percent difference is strongly influenced by the dynamic range of the measurements, with smaller values generally causing larger relative differences. The frequency histograms shown in Fig. 12 demonstrate that the BB-DIAL produced substantially fewer measurements at low WVMR ( $< 3 \text{ g kg}^{-1}$ ) than did either the RL or the AERI. This is due to the shorter height range of the BB-DIAL as compared with either the RL or AERI, which produced more valid measurements higher in the troposphere with low WVMRs, as indicated in Fig. 7. For the two-way intercomparisons shown in Fig. 12, the mean percent difference between the RL and the radiosonde is 1.6%, and the mean percent difference between the AERI and the radiosonde is 8.5%. These values are larger than those obtained using the four-way intercomparison of Table 2. The differences are largely due to the effect of the smaller WVMR values that are present in the radiosonde, RL and AERI datasets but absent from the BB-DIAL dataset.

In addition to comparing the radiosondes to the BB-DIAL, RL, and AERI, we also compare the BB-DIAL directly to the RL and AERI. Figure 13 shows bias and correlation profiles for the BB-DIAL versus RL (Fig. 13a), and for the BB-DIAL versus the AERI (Fig. 13b). For these comparisons, the RL height and time grids are used as reference grids such that the BB-DIAL and AERI observations are linearly interpolated to the height grid of the RL. In the time dimension, we take the BB-DIAL and AERI profiles that occur closest in time to a given RL profile. The bias and correlation profiles are computed using a three-way comparison method in which we use only those time and height bins that contain valid estimates from the RL, BB-DIAL and AERI. This ensures that the bias and correlation profiles are all computed under the same meteorological conditions. In contrast to the radiosonde comparisons shown in Figs. 11 and 13, these comparisons include considerably more data since we are not restricted to the radiosonde launch times.

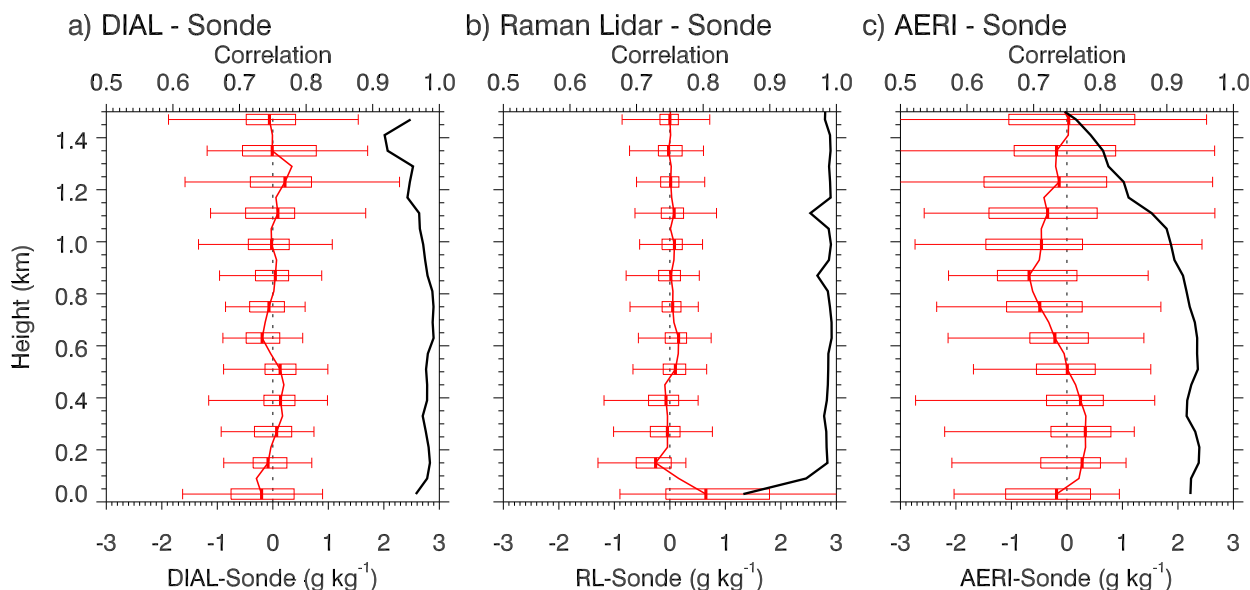


FIG. 11. Profiles of the median difference (red) and linear correlation coefficient (black) between the corrected radiosonde and (a) the BB-DIAL, (b) the RL, and (c) the AERI WVMR measurements. The profiles were generated using the four-way intercomparison method that is described in the text. Rectangles represent the 25th–75th-percentile range, and the whiskers represent the 5th–95th-percentile range. The number of radiosonde profiles used in these comparisons was 106.

The bias profile for the BB-DIAL-versus-RL comparison (Fig. 13a) remains between roughly  $-0.2$  and  $0.3 \text{ g kg}^{-1}$  with the exception of the lowest two range gates. These gates, which show relatively large negative biases, are likely affected by uncompensated overlap in the RL data. With the exception of the lowest range gate, the correlation profile in Fig. 13a stays above 0.9, although it decreases gradually from  $>0.95$  at  $\sim 800 \text{ m}$  to about 0.9 at 1500 m. The correlation profile for the BB-DIAL-versus-AERI comparison (Fig. 10b) remains roughly constant, at  $\sim 0.95$  below about 800 m. Above this level the correlation decreases dramatically to about 0.62 at 1500 m.

Frequency histograms of the RL and AERI versus the radiosonde are shown in Fig. 14. The standard deviations and correlation coefficients are similar, but the biases are very different, as indicated in the figure. The bias between the RL and the BB-DIAL is  $-0.04 \text{ g kg}^{-1}$ , and the bias between the AERI and the BB-DIAL is considerably larger at  $0.25 \text{ g kg}^{-1}$ . We also note that the AERI regression analysis indicates a tendency for the AERI to underestimate the WVMR relative to the BB-DIAL with increasing WVMR. However, this appears to be due to the influence of outliers in the dataset, as the highest concentration of measurements shown Fig. 14b closely follows the one-to-one line.

As noted previously, the near- and far-range spectral widths were adjusted in post processing in order to optimize the agreement between the radiosonde and the

BB-DIAL WVMR measurements. This optimization process used data from the current field campaign and two other campaigns that were conducted in 2017. Once determined, these spectral widths were used to process all of the BB-DIAL measurements during the current campaign and the other campaigns in 2017.

The stability of the calibration was evaluated by analyzing the daily mean percent difference between the BB-DIAL and radiosonde WVMR measurements over the duration of the current campaign. Any significant

TABLE 2. Statistics summarizing the comparisons between the corrected radiosonde (“sonde”) and the other instruments. Statistics were computed using the four-way intercomparison approach described in the text. Statistics include the mean difference (bias), the standard deviation of the difference (stDev), the Pearson linear correlation coefficient (Corr), the mean percent difference, and the slope and offset from linear regression analyses. The number of valid sample pairs used in each comparison was 1655. The corrected radiosonde data refer to RS92 measurements that have undergone the SRDB corrections and scaling by the MWR PWV.

	BB-DIAL-sonde	RL-sonde	AERI-sonde
Bias ( $\text{g kg}^{-1}$ )	-0.01	0.07	-0.23
StDev ( $\text{g kg}^{-1}$ )	0.65	0.74	1.23
Corr	0.98	0.97	0.92
Slope	0.94	0.97	0.87
Offset ( $\text{g kg}^{-1}$ )	0.59	0.34	1.00
Mean percent difference (%)	0.42	0.87	-2.0

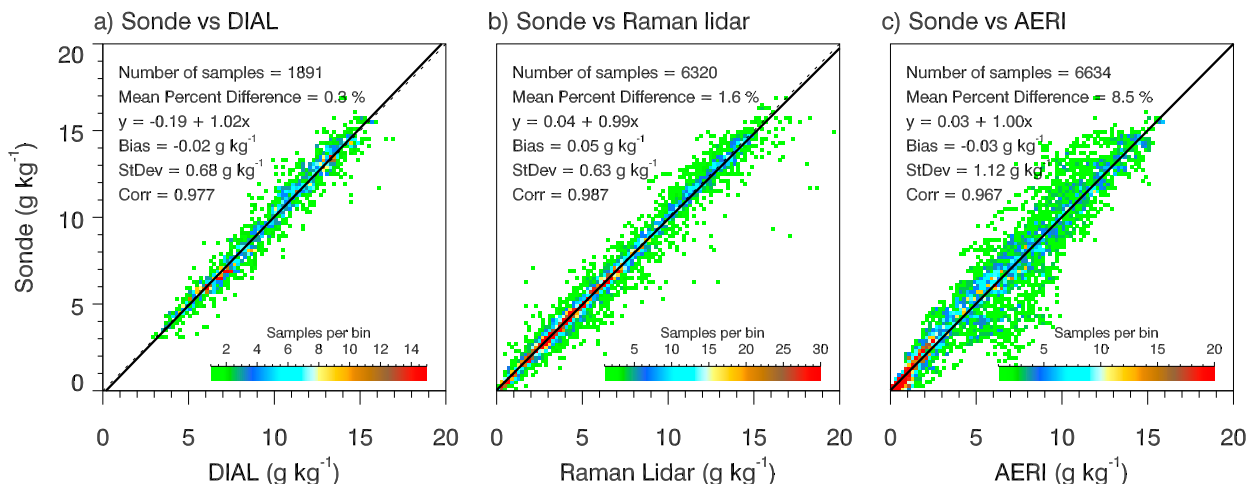


FIG. 12. Frequency histograms showing the correlation between the corrected radiosonde and (a) the BB-DIAL, (b) the RL, and (c) the AERI. The diagonal dashed lines show the ideal one-to-one relationship, and the solid black lines show the result of the linear regression analyses. Colors indicate the number of sample pairs per bin, where the bin size is  $0.2 \text{ g kg}^{-1} \times 0.2 \text{ g kg}^{-1}$ . Plots were generated using the two-way intercomparison approach that is described in the text.

long-term drift in the calibration should manifest itself as a detectable increase in the bias over time.

The daily mean percent difference was computed using all available radiosonde profiles on a given day, and using height bins between 100 and 800 m, where the BB-DIAL performance was optimal. A linear trend analysis was then performed by fitting a straight line (using least squares) to the daily mean percent differences. The result of this analysis, which is shown in Fig. 15, gives a trend line with a slope of  $+0.08\% \text{ day}^{-1}$ , but with considerable scatter in the day-to-day bias values.

The method outlined in Santer et al. (2000) was used to determine if the slope of the trend line shown in Fig. 15 is significantly different from zero. The so-called null hypothesis is that the slope could be zero by chance given the observed variability in Fig. 15. To accept or reject this hypothesis, we compute the Student's  $t$  score and compare that value with the critical  $t$  value corresponding to a prescribed significance level and degrees of freedom (DOF). In Fig. 15 there were 28 samples in the time series, giving  $\text{DOF} = 26$ . However, when we account for autocorrelation effects (Santer et al. 2000) the effective DOF becomes 12. The critical  $t$  for a confidence level of 80% and  $\text{DOF} = 12$  is 1.4. To reject the null hypothesis, the Student's  $t$  value must be equal to or greater than the critical  $t$  value. For the time series shown in Fig. 15, the Student's  $t$  score was determined to be 1.0. Thus, we cannot reject the null hypothesis (i.e., the possibility that the trend line slope could have been zero by chance), and so we conclude that the bias shows no statistically significant trend over the duration of the month-long field campaign. We note that we have based

this conclusion on the use of the 80% confidence level, as opposed to the more commonly used 95% confidence level, which imposes a more restrictive criterion for rejecting the null hypothesis.

#### 4. Summary

This study demonstrated the ability of a broadband DIAL system to run autonomously over an extended period of time while providing accurate height- and time-resolved measurements of humidity in the lower

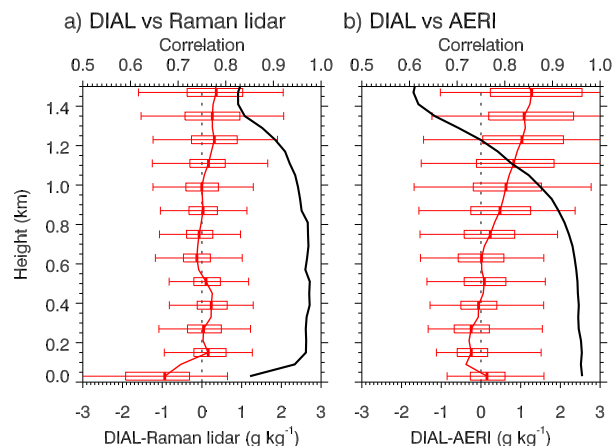


FIG. 13. Profiles of the median difference (red) and linear correlation coefficient (black) between the BB-DIAL and (a) the RL and (b) the AERI WVMR measurements. Also indicated by the box and whiskers are the 25th–75th and the 5th–95th percentiles of the differences. The number of profiles used in each panel was 4320. The plots were generated using the three-way intercomparison method that is described in the text.

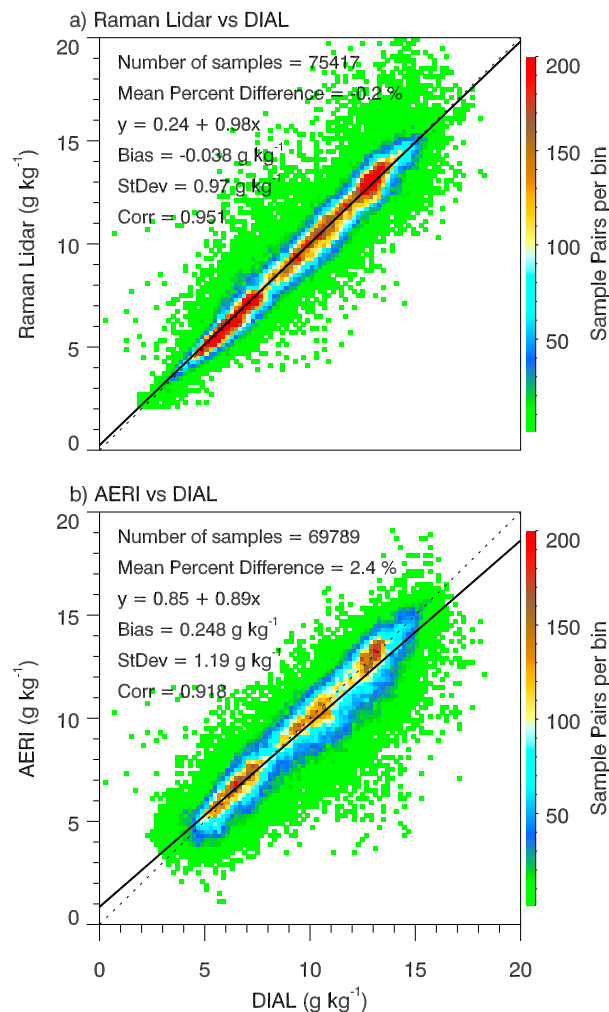


FIG. 14. Frequency histograms showing the correlation between the BB-DIAL and (a) the RL and (b) the AERI WVMR measurements. The diagonal dashed lines show the ideal one-to-one relationship, and the solid black lines show the result of the linear regression analyses. Colors indicate the number of sample pairs per bin, where the bin size is  $0.2 \text{ g kg}^{-1} \times 0.2 \text{ g kg}^{-1}$ . The plots were generated using the two-way intercomparison method that is described in the text.

troposphere. We provided an overview of the design of a prototype system developed by Vaisala and presented results from a month-long field trial of the system.

The Vaisala prototype was designed to provide height-resolved measurements of humidity in the lower troposphere. The temporal resolution is 20 min, with profiles reported every 2 min, and the height resolution varies from 10 m at the surface to 500 m at 3000 m AGL, with humidity values reported every 10 m. For the evaluation, the BB-DIAL was deployed at the SGP central facility from 15 May to 12 June 2017 to test its performance under the humid conditions that are typically encountered at SGP in the spring. During this

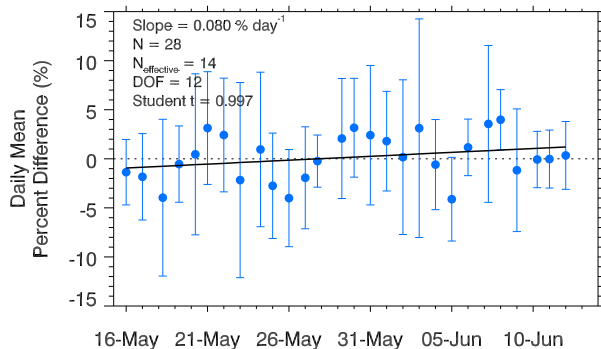


FIG. 15. Daily mean percent difference between the BB-DIAL and radiosonde vs time (blue filled circles). Differences were computed for height bins between 100 and 800 m. The solid black line shows the result of a linear regression. The Student's  $t$  value is 1.0 for this time series. The critical  $t$  value is 1.4 for  $\text{DOF} = 12$  and an 80% confidence level that the observed trend is significant. Since the  $t$  value is below the critical  $t$  value, we conclude that the slope of the observed trend is not significantly different from zero.

period, the BB-DIAL operated continuously and did not experience any failures or malfunctions.

BB-DIAL estimates of WVMR were compared with those from a collocated RL and AERI, and to RS92 radiosondes that were launched within 250 m of the BB-DIAL's location. The Wang et al. (2013) SRDB correction was applied to the RS92 data, and the SRDB-corrected profiles were scaled in order to match PWV measurement from a nearly collocated MWR.

The range performance of the BB-DIAL was assessed by examining the data availability as a function of height. We found that the BB-DIAL produces valid estimates greater than 50% of the time for heights less than 1200 m. During the field campaign, the daily mean maximum boundary layer height  $z_i$  was approximately 1600 m, and the percentage of valid measurements occurring at or below  $z_i$  was found to be 83%. Most of the missing values below  $z_i$  occur during afternoon periods when the boundary layer is near its maximum depth.

In comparing the BB-DIAL with the radiosonde we found the BB-DIAL measurements to be essentially unbiased ( $-0.01 \text{ g kg}^{-1}$ ) with a standard deviation of  $0.65 \text{ g kg}^{-1}$  and linear correlation coefficient of 0.98. This compares very well to the performance of the Raman lidar, which was also essentially unbiased with a standard deviation of  $0.74 \text{ g kg}^{-1}$  and a correlation coefficient of 0.97. When interpreting these results, it is important to note that neither the BB-DIAL nor the RL results are independent of the radiosonde. In the case of the RL, a height-dependent calibration profile was derived by comparing the RL data to radiosonde measurements taken over the duration of the current field campaign. In the case of the BB-DIAL, the near- and



far-range spectral widths were adjusted to optimize agreement with radiosonde data collected during the current field campaign and two other campaigns in 2017.

The BB-DIAL's WVMR measurements also compared favorably with the AERI-retrieved water vapor profiles, whose calibration was independent of the radiosondes. The AERI is a passive radiometer with a much coarser vertical resolution than the other instruments, yet the relatively small bias ( $-0.22 \text{ g kg}^{-1}$ ) and high correlation (0.92) between the BB-DIAL and AERI measurements provides additional confirmation that both instruments are able to capture the evolution of water vapor in the boundary layer with similar skill.

It is possible for the characteristics of the BB-DIAL's diode laser sources to change over time. This would require periodic recalibration of the laser spectra (i.e., adjustment of the spectral widths) using either direct laboratory measurements or using profiles of humidity from some suitable reference (e.g., radiosondes). However, for this study only one pair of spectral width values were used for the duration of the current field campaign, with no statistically significant trend observed in the humidity bias over time.

In another recent study, Weckwerth et al. (2016) performed a similar evaluation of a water vapor DIAL system, the MicroPulse DIAL (MPD), developed by Montana State University and the National Center for Atmospheric Research (Nehrir et al. 2012; Spuler et al. 2015). In that study, the mean percent difference was used to quantify the bias between the MPD and radiosonde data during two different field campaigns: the Plains Elevated Convection at Night (PECAN; Geerts et al. 2017) and the Front Range Air Pollution and Photochemistry Experiment (FRAPPE; Flocke et al. 2015). In these field campaigns the MPD used an integration time of 5 min, and the maximum height for valid measurements generally varied between 3 and 6 km. During the FRAPPE field study, the mean percent difference for the MPD-versus-radiosonde comparison was less than 3% for heights below 1.25 km, and during PECAN the mean percent difference was less than 10% for heights below 2.75 km. For the Vaisala BB-DIAL in the current study, the maximum height for valid measurements generally varied between 1000 and 1500 m and the mean percent difference with radiosonde measurements was found to be 0.4%. Superficially, these results suggest that the Vaisala BB-DIAL provides greater accuracy but with much less range than the MPD. However, such a conclusion cannot be made given the differences in meteorological conditions, radiosonde collocation and instrument configuration between the two studies. Also, because of its longer range the MPD likely produced a higher percentage of

low WVMR measurements compared to the Vaisala BB-DIAL in the current study. The prevalence of low WVMR values in the dataset would tend to increase the mean percent difference. An assessment of the relative performance of the Vaisala BB-DIAL and MPD can only be made by operating the two systems side by side over the same time period and by comparing the retrieved WVMR data to the same collocated reference measurements, for example, radiosondes.

The Vaisala BB-DIAL used in this study was previously evaluated during field campaigns in Germany, Finland (Roininen and Munkel 2017; Munkel and Roininen 2017), and in the tropics in Hong Kong. Although the system continues to evolve, results obtained in these other campaigns are generally consistent with those found in the current campaign. During the campaigns in Germany and Finland, the Vaisala BB-DIAL was able to measure WVMR with an absolute deviation of less than  $0.4 \text{ g kg}^{-1}$  up to roughly 1600 m. The current study, however, provides a much more comprehensive analysis of the performance.

Development efforts continue and new field campaigns are being conducted with the cooperation of Environment and Climate Change Canada (ECCC) and Deutscher Wetterdienst (DWD). ECCC has installed one BB-DIAL unit in the Arctic in Iqaluit, Canada, and DWD has installed another unit in Lindenberg, Germany. With these campaigns the performance of these systems can be evaluated under conditions different from the SGP site. Vaisala's plan for the final product is to incorporate characteristics of a multipurpose high-end ceilometer and add additional output data products such as attenuated backscatter profiles and measurements of cloud-base height up to 15 km.

*Acknowledgments.* This research was supported by the Office of Biological and Environmental Research of the U.S. Department of Energy as part of the Atmospheric Radiation Measurement Climate Research Facility. We also express our appreciation to the staff at the ARM SGP site. A portion of this work was supported by the NOAA Atmospheric Science for Renewable Energy (ASRE) program.

## REFERENCES

- Ansmann, A., M. Riebesell, and C. Weitkamp, 1990: Measurement of atmospheric aerosol extinction profiles with a Raman lidar. *Opt. Lett.*, **15**, 746–748, <https://doi.org/10.1364/OL.15.000746>.
- Bartholomew, M. J., 2016: Impact disdrometer instrument handbook. U.S. Dept. of Energy Doc. DOE/SC-ARM-TR-111, 12 pp., [https://www.arm.gov/publications/tech\\_reports/handbooks/disdrometer\\_handbook.pdf](https://www.arm.gov/publications/tech_reports/handbooks/disdrometer_handbook.pdf).

- Benjamin, S. G., and Coauthors, 2016: A North American hourly assimilation and model forecast cycle: The Rapid Refresh. *Mon. Wea. Rev.*, **144**, 1669–1694, <https://doi.org/10.1175/MWR-D-15-0242.1>.
- Berg, L. K., R. K. Newsom, and D. D. Turner, 2017: Year-long vertical velocity statistics derived from Doppler lidar in the continental convective boundary layer. *J. Appl. Meteor. and Climatol.*, **56**, 2441–2454, <https://doi.org/10.1175/JAMC-D-16-0359.1>.
- Blumberg, W. G., D. D. Turner, U. Löhnert, and S. Castleberry, 2015: Ground-based temperature and humidity profiling using spectral infrared and microwave observations. Part II: Actual retrieval performance in clear-sky and cloudy conditions. *J. Appl. Meteor. Climatol.*, **54**, 2305–2319, <https://doi.org/10.1175/JAMC-D-15-0005.1>.
- Bucholtz, A., 1995: Rayleigh-scattering calculations for the terrestrial atmosphere. *Appl. Opt.*, **34**, 2765–2773, <https://doi.org/10.1364/AO.34.002765>.
- Cadeddu, M. P., J. C. Liljegen, and D. D. Turner, 2013: The Atmospheric Radiation Measurement (ARM) program network of microwave radiometers: Instrumentation, data, and retrievals. *Atmos. Meas. Tech.*, **6**, 2359–2372, <https://doi.org/10.5194/amt-6-2359-2013>.
- Cady-Pereira, K. E., M. W. Shephard, D. D. Turner, E. J. Mlawer, S. A. Clough, and T. J. Wagner, 2008: Improved daytime column-integrated precipitable water vapor from Vaisala radiosonde humidity sensors. *J. Atmos. Oceanic Technol.*, **25**, 873–883, <http://doi.org/10.1175/2007JTECHA1027.1>.
- Dabberdt, W., and Coauthors, 2016: Advances in continuous atmospheric boundary layer humidity profiling with a compact DIAL Instrument. *18th Symp. on Meteorological Observation and Instrumentation*, New Orleans, LA, Amer. Meteor. Soc., 8.4, <https://ams.confex.com/ams/96Annual/webprogram/Paper285586.html>.
- Dinoyev, T., V. Simeonov, Y. Arshinov, S. Bobrovnikov, P. Ristori, B. Calpini, M. Parlange, and H. van den Bergh, 2013: Raman lidar for meteorological observations, RALMO—Part 1: Instrument description. *Atmos. Meas. Tech.*, **6**, 1329–1346, <https://doi.org/10.5194/amt-6-1329-2013>.
- Dzambo, A. M., D. D. Turner, and E. J. Mlawer, 2016: 2016: Evaluation of two Vaisala RS92 radiosonde solar radiative dry bias correction algorithms. *Atmos. Meas. Tech.*, **9**, 1613–1626, <https://doi.org/10.5194/amt-9-1613-2016>.
- Feltz, W. F., W. L. Smith, H. B. Howell, R. O. Knuteson, H. Woolf, and H. E. Revercomb, 2003: Near-continuous profiling of temperature, moisture, and atmospheric stability using the Atmospheric Emitted Radiance Interferometer (AERI). *J. Appl. Meteor.*, **42**, 584–597, [https://doi.org/10.1175/1520-0450\(2003\)042<0584:NPOTMA>2.0.CO;2](https://doi.org/10.1175/1520-0450(2003)042<0584:NPOTMA>2.0.CO;2).
- Flocke, F., and Coauthors, 2015: The Front Range Air Pollution and Photochemistry Experiment (FRAPPE)—An overview. *2015 Fall Meeting*, San Francisco, CA, Amer. Geophys. Union, Abstract A12A-01.
- Foth, A., H. Baars, P. Di Girolamo, and B. Pospichal, 2015: Water vapour profiles from Raman lidar automatically calibrated by microwave radiometer data during HOPE. *Atmos. Chem. Phys.*, **15**, 7753–7763, <https://doi.org/10.5194/acp-15-7753-2015>.
- Geerts, B., and Coauthors, 2017: The 2015 Plains Elevated Convection at Night field project. *Bull. Amer. Meteor. Soc.*, **98**, 767–786, <https://doi.org/10.1175/BAMS-D-15-00257.1>.
- Goldsmith, J. E. M., F. H. Blair, S. E. Bisson, and D. D. Turner, 1998: Turn-key Raman lidar for profiling atmospheric water vapor, clouds and aerosols. *Appl. Opt.*, **37**, 4979–4990, <https://doi.org/10.1364/AO.37.004979>.
- Holben, B. N., and Coauthors, 1998: AERONET—A federated instrument network and data archive for aerosol characterization. *Remote Sens. Environ.*, **66**, 1–16, [https://doi.org/10.1016/S0034-4257\(98\)00031-5](https://doi.org/10.1016/S0034-4257(98)00031-5).
- Knuteson, R. O., and Coauthors, 2004a: The Atmospheric Emitted Radiance Interferometer. Part I: Instrument design. *J. Atmos. Oceanic Technol.*, **21**, 1763–1776, <https://doi.org/10.1175/JTECH-1662.1>.
- , and Coauthors, 2004b: The Atmospheric Emitted Radiance Interferometer. Part II: Instrument performance. *J. Atmos. Oceanic Technol.*, **21**, 1777–1789, <https://doi.org/10.1175/JTECH-1663.1>.
- Le Hoai, P. P., M. Abo, and T. Sakai, 2016: Development of field-deployable diode-laser-based water vapor DIAL. *EJP Web Conf.*, **119**, 05011, <https://doi.org/10.1051/epjconf/201611905011>.
- Löhnert, U., D. D. Turner, and S. Crewell, 2009: Ground-based temperature and humidity profiling using spectral infrared and microwave observations. Part I: Simulated retrieval performance in clear-sky conditions. *J. Appl. Meteor. Climatol.*, **48**, 1017–1032, <https://doi.org/10.1175/2008JAMC2060.1>.
- Mather, J. H., and J. W. Voyles, 2013: The Arm Climate Research Facility: A review of structure and capabilities. *Bull. Amer. Meteor. Soc.*, **94**, 377–392, <https://doi.org/10.1175/BAMS-D-11-00218.1>.
- Miloshevich, L. M., H. Vömel, D. N. Whiteman, and T. Leblanc, 2009: Accuracy assessment and correction of Vaisala RS92 radiosonde water vapor measurements. *J. Geophys. Res.*, **114**, D11305, <https://doi.org/10.1029/2008JD011565>.
- Mlawer, E. J., and D. D. Turner, 2016: Spectral radiation measurements and analysis in the ARM program. *The Atmospheric Radiation Measurement Program: The First 20 Years*, Meteor. Monogr., No. 57, Amer. Meteor. Soc., <https://doi.org/10.1175/AMSMONOGRAPHS-D-15-0027.1>.
- , V. H. Payne, J.-L. Moncet, J. S. Delamere, M. J. Alvarado, and D. C. Tobin, 2012: Development and recent evaluation of the MT\_CKD model of continuum absorption. *Philos. Trans. Roy. Soc. London*, **370A**, 2520–2556, <https://doi.org/10.1098/rsta.2011.0295>.
- Münkel, C., and R. Roininen, 2017: Results from continuous atmospheric boundary layer humidity profiling with a compact DIAL instrument. *EMS Annual Meeting Abstracts*, Vol. 14, EMS2017-525, <https://meetingorganizer.copernicus.org/EMS2017/EMS2017-525.pdf>.
- Nehrir, A. R., K. S. Repasky, and J. L. Carlsten, 2012: Micropulse water vapor differential absorption lidar: Transmitter design and performance. *Opt. Express*, **20**, 25 137–25 151, <https://doi.org/10.1364/OE.20.025137>.
- Newsom, R. K., D. D. Turner, B. Mielke, M. F. Clayton, R. Ferrare, and C. Sivaraman, 2009: Simultaneous analog and photon counting detection for Raman lidar. *Appl. Opt.*, **48**, 3903–3914, <https://doi.org/10.1364/AO.48.003903>.
- , —, and J. E. M. Goldsmith, 2013: Long-term evaluation of temperature profiles measured by an operational Raman lidar. *J. Atmos. Oceanic Technol.*, **30**, 1616–1634, <https://doi.org/10.1175/JTECH-D-12-00138.1>.
- NRC, 2009: *Observing Weather and Climate from the Ground Up: A Nationwide Network of Networks*. National Academies Press, 250 pp., <https://doi.org/10.17226/12540>.
- , 2010: *When Weather Matters: Science and Service to Meet Critical Societal Needs*. National Academies Press, 198 pp., <https://doi.org/10.17226/12888>.

- , 2012: *Weather Services for the Nation: Becoming Second to None*. National Academies Press, 86 pp., <https://doi.org/10.17226/13429>.
- Povey, I. M., A. M. South, A. De Roodenbeke, C. Hill, R. A. Freshwater, and R. L. Jones, 1998: A broadband lidar for measurement of tropospheric constituent profiles from the ground. *J. Geophys. Res.*, **103**, 3369–3380, <https://doi.org/10.1029/97JD02969>.
- Reichardt, J., U. Wandinger, V. Klein, I. Mattis, B. Hilber, and R. Begbie, 2012: RAMSES: German Meteorological Service autonomous Raman lidar for water vapor, temperature, aerosol, and cloud measurements. *Appl. Opt.*, **51**, 8111–8131, <https://doi.org/10.1364/AO.51.008111>.
- Roininen, R., and C. Münkel, 2017: Results from continuous atmospheric boundary layer humidity profiling with a compact DIAL instrument. *Eighth Symp. on Lidar Atmospheric Applications*, Seattle, WA, Amer. Meteor. Soc., 12.3, <https://ams.confex.com/ams/97Annual/webprogram/Paper301717.html>.
- Rose, T., S. Crewell, U. Löhnert, and C. Simmer, 2005: A network suitable microwave radiometer for operational monitoring of the cloudy atmosphere. *Atmos. Res.*, **75**, 183–200, <https://doi.org/10.1016/j.atmosres.2004.12.005>.
- Rothman, L. S., and Coauthors, 2009: The HITRAN 2008 Molecular Spectroscopic Database. *J. Quant. Spectrosc. Radiat. Transfer*, **110**, 533–572, <https://doi.org/10.1016/j.jqsrt.2009.02.013>.
- Santer, B. D., T. M. L. Wigley, J. S. Boyle, D. J. Gaffen, J. J. Hnilo, D. Nychka, D. E. Parker, and K. E. Taylor, 2000: Statistical significance of trends and trend differences in layer-average atmospheric temperature time series. *J. Geophys. Res.*, **105**, 7337–7356, <https://doi.org/10.1029/1999JD901105>.
- Sisterson, D. L., R. A. Pepler, T. S. Cress, P. J. Lamb, and D. D. Turner, 2016: The ARM Southern Great Plains (SGP) site. *The Atmospheric Radiation Measurement Program: The First 20 Years*, Meteor. Monogr., No. 57, Amer. Meteor. Soc., <https://doi.org/10.1175/AMSMONOGRAPHIS-D-16-0004.1>.
- Solheim, F., J. Godwin, E. Westwater, Y. Han, S. Keihm, K. Marsh, and R. Ware, 1998: Radiometric profiling of temperature, water vapor, and cloud liquid water using various inversion methods. *Radio Sci.*, **33**, 393–404, <https://doi.org/10.1029/97RS03656>.
- South, A. M., I. M. Povey, and R. L. Jones, 1998: Broadband lidar measurements of tropospheric water vapor profiles. *J. Geophys. Res.*, **103**, 31 191–31 202, <https://doi.org/10.1029/98JD02852>.
- Spuler, S. M., K. S. Repasky, B. Morley, D. Moen, M. Hayman, and A. R. Nehrir, 2015: Field-deployable diode-laser-based differential absorption lidar (DIAL) for profiling water vapor. *Atmos. Meas. Tech.*, **8**, 1073–1087, <https://doi.org/10.5194/amt-8-1073-2015>.
- Steinbrecht, W., H. Claude, F. Schönenborn, U. Leiterer, H. Dier, and E. Lanzinger, 2008: Pressure and temperature differences between Vaisala RS80 and RS92 radiosonde systems. *J. Atmos. Oceanic Technol.*, **25**, 909–927, <https://doi.org/10.1175/2007JTECHA999.1>.
- Turner, D. D., and J. E. M. Goldsmith, 1999: Twenty-Four-Hour Raman lidar water vapor measurements during the Atmospheric Radiation Measurement program's 1996 and 1997 water vapor intensive observation periods. *J. Atmos. Oceanic Technol.*, **16**, 1062–1076, [https://doi.org/10.1175/1520-0426\(1999\)016<1062:TFHRLW>2.0.CO;2](https://doi.org/10.1175/1520-0426(1999)016<1062:TFHRLW>2.0.CO;2).
- , and U. Löhnert, 2014: Information content and uncertainties in thermodynamic profiles and liquid cloud properties retrieved from the ground-based Atmospheric Emitted Radiance Interferometer (AERI). *J. Appl. Meteor. Climatol.*, **53**, 752–771, <https://doi.org/10.1175/JAMC-D-13-0126.1>.
- , and W. G. Blumberg, 2019: Improvements to the AERIE thermodynamic profile retrieval algorithm. *IEEE Sel. Top. Appl. Earth Obs. Remote Sens.*, **12**, 1339–1354, <https://doi.org/10.1109/JSTARS.2018.2874968>.
- , B. M. Lesht, S. A. Clough, J. C. Liljegren, H. E. Revercomb, and D. C. Tobin, 2003: Dry bias and variability in Vaisala radiosondes: The ARM experience. *J. Atmos. Oceanic Technol.*, **20**, 117–132, [https://doi.org/10.1175/1520-0426\(2003\)020<0117:DBAIVV>2.0.CO;2](https://doi.org/10.1175/1520-0426(2003)020<0117:DBAIVV>2.0.CO;2).
- , R. O. Knuteson, and H. E. Revercomb, 2006: Noise reduction of Atmospheric Emitted Radiance Interferometer (AERI) observations using principal component analysis. *J. Atmos. Oceanic Technol.*, **23**, 1223–1238, <https://doi.org/10.1175/JTECH1906.1>.
- , J. E. M. Goldsmith, and R. A. Ferrare, 2016: Development and applications of the ARM Raman lidar. *The Atmospheric Radiation Measurement Program: The First 20 Years*, Meteor. Monogr., No. 57, Amer. Meteor. Soc., <https://doi.org/10.1175/AMSMONOGRAPHIS-D-15-0026.1>.
- Wang, J., L. Zhang, A. Dai, F. Immler, M. Sommer, and H. Vomel, 2013: Radiation dry bias correction of Vaisala RS92 humidity data and its impacts on historical radiosonde data. *J. Atmos. Oceanic Technol.*, **30**, 197–214, <https://doi.org/10.1175/JTECH-D-12-00113.1>.
- Weckwerth, T. M., K. J. Weber, D. D. Turner, and S. M. Spuler, 2016: Validation of a water vapor micropulse differential absorption lidar (DIAL). *J. Atmos. Oceanic Technol.*, **33**, 2353–2372, <https://doi.org/10.1175/JTECH-D-16-0119.1>.
- Weitekamp, C., Ed., 2005: *Lidar: Range-Resolved Optical Remote Sensing of the Atmosphere*. Springer, 456 pp., <https://doi.org/10.1007/b106786>.
- Whiteman, D. N., 2003: Examination of the traditional Raman lidar technique. II. Evaluating the ratios for water vapor and aerosols. *Appl. Optics*, **42**, 2593–2608, <https://doi.org/10.1364/ao.42.002593>.
- , S. H. Melfi, and R. A. Ferrare, 1992: Raman lidar system for the measurement of water vapor and aerosols in the Earth's atmosphere. *Appl. Opt.*, **31**, 3068–3082, <https://doi.org/10.1364/AO.31.003068>.
- Wulfmeyer, V., and Coauthors, 2015: A review of the remote sensing of lower tropospheric thermodynamic profiles and its indispensable role for the understanding and the simulation of water and energy cycles. *Rev. Geophys.*, **53**, 819–895, <https://doi.org/10.1002/2014RG000476>.